Universitat Autònoma de Barcelona
Institut de Física d'Altes Energies

The Atmospheric Density Profile influence on IACT

Treball de Reserca de Màster

Cosme Adrover Pacheco

Supervised by Lluis Font and Abelardo Moralejo

Barcelona, July 2009

Contents

Chapter 1

Introduction

Astroparticle physics is a new interdisciplinary and rapidly expanding area, which combines the experimental techniques and theoretical methods from both astronomy and particle physics. The most active topics in Astroparticle physics are:

- γ-ray astronomy,
- Search for dark matter,
- Detailed studies of cosmic rays,
- Neutrino physics and neutrino astronomy,
- Search for gravitational waves.

This master's thesis work is under the field of γ-ray astronomy.

Observational astronomy has evolved over many centuries just observing astronomical objects that emit radiation in the optical frequency band. In the 20^{th} century, radio astronomy -on the lower edge of the spectrum- and X-ray astronomy -on the upper band- have proven that much information can be extracted by studying the radiation that comes from astrophysical objects in a wider energy range.

Any radiation emitted beyond the X-ray band of the spectrum can not be originated by thermal radiation processes but involves the production and acceleration of highly relativistic particles that originate in extremely violent astrophysical environments such as active galactic nuclei, supernova remnants, pulsars, gamma-ray bursts or microquasars. Among all the highly energetic particles that these processes generate, just gamma-rays and neutrinos are not affected by the interestellar and intergalactic magnetic fields, and, therefore, can be traced back to their production sites, acting as messengers of distant cosmic events.

The γ-ray astronomy is one of the youngest branches of Astroparticle physics. Though it was realized by Viktor Hess already in 1912 [1] that the earth was constantly bombarded by a flux of high energy cosmic rays (which are mostly relativistic protons), it took more than 50 years to learn how to efficiently detect the electromagnetic part of cosmic rays: the γ-rays. There are two ways of detecting gamma-rays of cosmic origin: studying the particle showers they induce in the atmosphere, or directly, by putting a gamma-ray detector on a satellite. The number of γ-rays coming from celestial objects usually decreases with increasing energy, which means that γ-rays at high energies (E $>$ 100 MeV) are very difficult to be detected with satellites, since their effective area is limited (usually to less than a square meter). It is from hundreds of GeV, and specially in the TeV region, where ground-based detectors have a very high performance in detecting the secondary particles produced in the air showers and reconstructing the cascade development[1] to estimate the origin and the energy of the primary gamma-ray.

The ground-based γ-ray astronomy based on the study of the air shower products using Imaging Air Cherenkov Telescopes (IACT) started with the first detection of a TeV source by *WHIPPLE* telescope (10 m ϕ) ,already in 1989 [2], and stablishing the Crab-Nebula as a VHE emitter. In the 1990s, the *HEGRA* collaboration followed *WHIPPLE* by constructing a series of smaller telescopes, and achieving an improvement on the reconstruction capabillity. But it has been in the last decade, when a new generation of Cherenkov telescopes (*MAGIC*, *HESS* and *VERITAS*) has pushed down the detection energy threshold and sensitivity, increasing almost exponentially the number of detected GeV and TeV sources.

The Major Atmospheric Gamma-ray Imaging Cherenkov telescope MAGIC is currently the largest of its kind operating in the world, with 17 m diameter and $236\,m^2$ of mirror area, and has been in operation since late 2004. *MAGIC* was designed to be a discovery telescope, having the lowest energy threshold among the instruments of its generation. It is located at the Roque de los Muchachos Observatory in the island of La Palma (Canary Islands, Spain) at 2200 m above the sea level.

The aim of this study is to estimate (via simulation) the effects of atmosphere composition on current IACT and future projects as the Cherenkov Telescope Array (*CTA*) project. The *CTA* is an initiative to build the next generation of ground-based gamma-ray instruments. The current baseline design of *CTA* was presented for the first time in fall 2005 to the European ESFRI[2] sub-comittee. The observatory will consist of two arrays: a southern hemisphere array, which covers the full energy range from some 10 GeV to about 100 TeV to allow for a deep investigation of galactic sources, and of the central part of our Galaxy, but also for the observation of extragalactic objects. A northern hemisphere array, consisting of the low energy instrumentation (from some 10 GeV to few 10's of GeV) complements the observatory and is dedicated mainly to extragalactic objects.

[1]This concept will be explained in chapter 2

[2]European Strategy Forum on Research Infrastructures

The atmospheric monitoring in Cherenkov experiments has always played an important role, since monitoring the properties of the atmosphere is essential for the interpretation of the Cherenkov signal, in terms of energy spectrum of the gamma rays and the time variation of source fluxes [15]. In this direction, several tests have been performed in the MAGIC collaboration, regarding the implementation of the amospheric density profiles and the resulting lateral distribution of Cherenkov photons in the MAGIC software [16] and, also, some attemps at correcting the results of the observations for the effect of non-optimal atmospheric conditions [17].

In the *CTA* meeting in Padova (Italy) in November 2008 Dr. Sam Nolan, member of the *HESS* collaboration and also an active member of CTA project, presented a brief discussion [6] about his recent work. In his presentation, Nolan showed that considering different atmospheric models (of density, temperature and refractive index) and, most importantly, different aerosol distributions (which act as a filter lowering the Cherenkov yield), a change in the expected energy spectrum of the Crab Nebula (the Standard Candle in VHE astrophysics) was observed. All these results where elaborated using the CTA simultation software over an array of 97 Cherenkov telescopes.

Based on these results the *MAGIC* groups at Universitat Autònoma de Barcelona and IFAE (High Energy Physics Institute), both at Bellaterra (Barcelona) decided to check Nolan's results using the software of the collaboration. On behalf of this, and using the MAGIC software (described later), I started my work studying two different molecular profiles, which will be complementary to the work to be done by D. Hrupec [20] regarding the aerosol influence. It is worth it to mention that, in the standard analysis chain of MAGIC, the Monte Carlo data used is generated with the atmospheric density profile of the US Standard atmosphere. In this sense, the main idea of the whole project is to estimate the consequences of using a diffent atmospheric density profile, which in this work is the Magic Winter, instead of the US Standard.

The supervisors of this master's project are Professor Dr. Lluis Font, who belongs to the CTA-ATAC group for the Atmospheric monitoring, associated science and instrumentation calibration and also is a member of the *MAGIC* collaboration at Universitat Autònoma de Barcelona, Bellaterra (Spain), and Dr. Abelardo Moralejo, who is a MAGIC member in IFAE, Bellaterra, and is the software coordinator of the MAGIC collaboration.

My dissertation follows the structure outlined bellow:

Chapter 2 gives a brief overview about γ-rays, their production and about their interaction with atmosphere. It is explained how the showers and the Cherenkov light are produced. Futhermore, the processes involved in the Cherenkov attenuation yield is described. Finally, the key elements of background rejection are introduced.

Chapter 3 is engaged in the simulation and analysis processes. The whole process is explained starting with the first collision of a cosmic ray with an atmospheric nucleus, following by its detection on the telescope, and finishing with its recognition.

Chapter 4 contains results of the different simulations for different atmospheric models. The obtained ratios of effective areas between the two models and the effect on the Crab Nebula Spectrum are presented and discussed.

Chapter 5 summarizes the results and gives an outlook.

Chapter 2

Very High Energy γ-ray Astrophysics

2.1 What are γ-rays and how are they produced?

The Earth's atmosphere is permanently bombarded by ionizing radiation. These so-called cosmic rays consist of 86% protons, 11% α-particles, 1% heavy nuclei, 2% electrons and, making up a fraction of cosmic rays as small as $< 10^{-4}$, γ's are present [3] [4].

Gamma-rays are electromagnetic radiation of very short wavelength of $\lambda < 10^{-11}$ m. These high energy photons have energies of more than 1 MeV up to several TeV. The definition of the different energy/wavelength bands of the electromagnetic spectrum is shown in figure 2.1.

Astronomical objects emit energy in different types of processes. In classical astronomy the universe turns out to be dominated by thermal radiation which can be described by a blackbody radiation (Planck's formula). Yet, already in the case of 1 MeV γ-rays, one would need temperatures in the order of $2 \cdot 10^9$ K (the sun's core shows a temperature in the order of 10^7 K) to explain their emission. Thus, the emission of γ-rays at VHE is dominated by nonthermal processes. The most relevant processes are shown in figure 2.2. Detailed explanations can be found in [3] and [5].

The **Inverse Compton Scattering** is thought to be the main production mechanism for VHE photons in astroparticle sources. In this process, relativistic electrons and positrons scatter off low energy photons and transfer parts of their energy to these photons.

2.2 Extensive Air Showers

Once high energy cosmic γ-rays enter the atmosphere of the Earth, they start to interact with particles in the atmosphere and produce large cascades with a huge

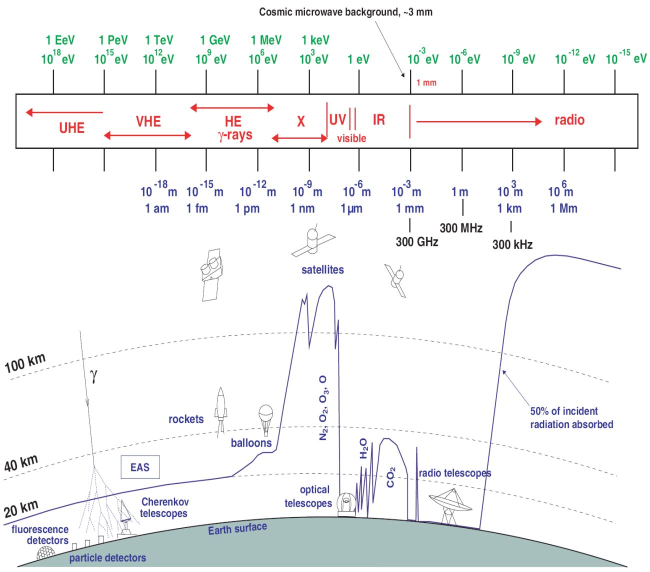

Figure 2.1: Atmospheric windows for electromagnetic radiation to observe the Universe. Common definitions of the energy bands are written in red. The continuous blue line corresponds to the height, at which a detector can receive half of the total incoming radiation at a given wavelength.

number of secondary particles (e^+,e^-,γ), called "Extensive Air Showers (EAS)". The γ-rays generate air showers via the electromagnetic interaction ("Electromagnetic cascade"). The energetic secondary charged particles emit Cherenkov radiation which can be detected with an IACT to obtain information of the primary γ-ray. Charged cosmic rays (protons, helium nuclei.. etc.) also induce Cherenkov light through the Eletromagnetic sub-showers of the "Hadronic cascade" and become background for the γ-ray observations with the IACT.

This chapter briefly summarizes the physics of air showers and describes the subsequent production of Cherenkov light.

2.2.1 Electromagnetic Cascade

The basic high energy processes making up an electromagnetic cascade are bremsstrahlung and pair production [3].

Bremsstrahlung: Bremsstrahlung is the radiation associated with the acceleration of electrons in the electrostatic fields of ions and nuclei of atoms. The energy loss per length X ([g/cm^2]) of a charged particle in the relavistic regime due to Bremsstrahlung can be described by:

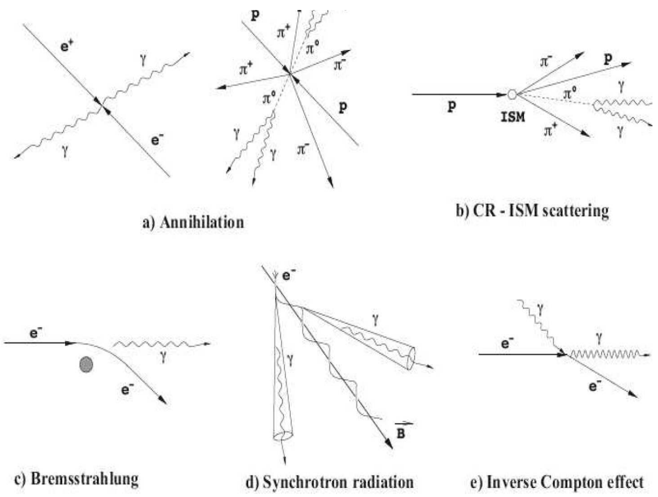

Figure 2.2: Schematic illustration of the main mechanisms of γ-ray production. The **I**nter**S**tellar **M**edium (ISM) or cosmic ray particles can be protons or heavy ions.

$$-\frac{dE}{dX} = 4\alpha N_A \frac{Z^2}{A} z^2 r_e^2 \left(\frac{m_e}{m}\right)^2 E\, ln \left(\frac{183}{Z^{1/3}}\right) \tag{2.1}$$

where $\alpha = \frac{e^2}{\hbar c} = \frac{1}{137}$ is the fine-structure constant, N_A is the Avogadro number, ρ, A and Z are the average density, atomic mass and charge of the medium, m_e is the electron mass, r_e is the classical electron radius and z, m and E are the incoming particle charge, mass and energy, respectively. The definition of radiation length X_0 comes from:

$$\frac{dE}{dX} = -\frac{E}{X_0} \;\; with \;\; X_0^{-1} = 4\alpha N_A \frac{Z^2}{A} z^2 r_e^2 \left(\frac{m_e}{m}\right)^2 E\, ln \left(\frac{183}{Z^{1/3}}\right) \tag{2.2}$$

The radiation length X_0 for electrons in air is 36.7 g/cm^2, corresponding to $\approx 300\, m$ for standard pressure at sea level.

Pair production: In this process, an electron-positron pair is produced by the interaction of a high energy photon with a virtual photon (γ^*) emitted in the strong electrostatic field of nuclei ($\gamma + \gamma^* \rightarrow e^+ + e^-$).

Both characteristic lenghts of bremsstrahlung and pair production can be expressed by X_0.

The EAS developes in an energy regime where bremsstrahlung and pair production are the dominating interaction mechanisms. The critical energy is defined as the energy where the contribution of these two processes equals the contribution of the rest of the physical processes in the EAS, and has a value in the atmosphere of $\sim$ 80 MeV. Once an electron falls bellow the critical energy it stops producing secondary photons by bremsstrahlung, however, it continues to lose its energy by ionization loss.

Primary cosmic γ-ray interact with nuclei and induce electron-positron pairs by the pair production process. Subsequently, the electrons and positrons emit γ-rays via bremsstrahlung, and then these γ-rays again produce electron-positron pairs. Air showers induced by γ-rays continue to develop through these electromagnetic cascades as long as the secondary particles have energies above the critical energy. Once the particles fall below the critical energy, ionization, excitation and Compton scattering dominate the energy loss and, finally, the cascade shower stops.

The shower development is strongly collimated towards the direction of the incident γ-ray. The total number of electrons and positrons above the critical energy E_c can be approximated by

$$N_e(t,E) = \frac{0.31}{\sqrt{ln\left(\frac{E}{E_c}\right)}} exp\left[t\left(1-\frac{3}{2}ln\, s\right)\right] \tag{2.3}$$

where E is the energy of the primary γ-ray, t is the depth of atmosphere scaled with respect to the radiation length ($t = \frac{X}{X_0}, X_0 = 36,7 g/cm^2$) , and s is called "shower *age*". The *age* parameter measures the evolution fo the shower in time, therefore when the shower starts this parameter equals 0, equals 1 at the maximum, and 2 when the mean number of particles is below one.

2.2.2 Hadronic cascade

Hadronic showers are produced by the interaction of high energy cosmic nuclei (mostly protons and helium nuclei) hitting an atmospheric nucleus governed by strong interacion. As a result of the interaction, pions, kaons and light baryons are produced. Since the π^0 has a short lifetime ($\tau \sim 8.3 \cdot 10^{-17}$ s), it decays to 2 γs as soon as it is created by the interaction, and these γ-rays induce electromagnetic cascades ("sub-showers"). Muons, comming from the decays $\pi^+ \rightarrow \mu^+ \nu_\mu$ and $\pi^- \rightarrow \mu^- \bar{\nu_\mu}$, have a relatively long lifetime ($\tau \sim 2.2 \cdot 10^6$ s) and they can decay through $\mu \rightarrow e + \nu_\mu \nu_e$ and also can induce an electromagnetic sub-shower.

Hadrons and pions give rise to hadronic cascades through further collisions, resulting in photons, electrons, positrons and muons, that develop electromagnetic sub-showers.

A hadronic shower grows until the energy per nucleon is below the pion production threshold (about 1GeV).

Fig 2.3 outlines the developmtents of EAS and Hadronic Showers. A lateral view of the simulated hadronic and EAS illustrates the fact that hadronic showers are broader, much wider and much more irregular than the electromagnetic ones (Fig. 2.4).

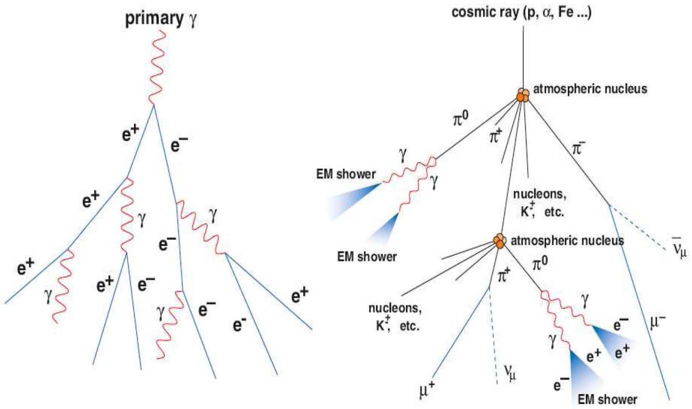

Figure 2.3: Sketch of the development of an EAS induced by a γ-ray (*left*) and by a charged cosmic nuleus (*right*).

2.3 Cherenkov Radiation

A charged particle passing through matter loses energy due to Coulomb interaction with the electrons of the matter. In general this energy is absorbed in the vicinity of the particle track. However if the particle velocity is faster than the local group velocity of light, part of the energy is emitted as radiation and can propagate through the matter in case of materials of high optical transmissivity. This radiation is called Cherenkov light and was discovered by P.A. Cherenkov in 1934 [8]. The theoretical explanation was given by Frank and Tamm in 1937 [9].

The emission of Cherenkov light is described by the superposition of spherical waves using Huygens' principle (see Fi. 2.5). The resulting cone-shaped wave-front has an angle of emission θ_c that can be deduced from geometrical considerations:

$$cos\theta_c = \frac{1}{\beta \cdot n} \tag{2.4}$$

2.3.1 Cherenkov radiation in air shower

As the refractive index depends on the density of the medium, it changes with the atmospheric altitude. Therefore, the Cherenkov emission angle and the energy threshold for Cherenkov production take different values along the path of the shower.

The refractive index of the air *n(h)* can be written as a function of the height h:

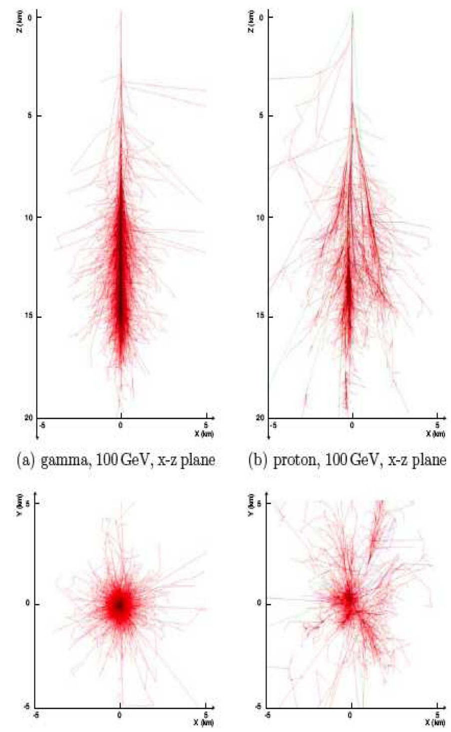

(a) gamma, 100 GeV, x-z plane (b) proton, 100 GeV, x-z plane

(c) gamma, 100 GeV, x-y plane (d) proton, 100 GeV, x-y plane

Figure 2.4: Simulated longitudinal (*top*) and lateral (*bottom*) developments of an electromagnetic (*left*) and hadronic (*right*) shower with initial energy of 100 GeV.

$$n(h) = 1 + \eta = 1 + \eta_0 \cdot exp\left(-\frac{h}{h_0}\right) \tag{2.5}$$

Given the fact that $\eta \ll 1$, the energy threshold can be written as:

$$E_{th} \approx \frac{m_0 c^2}{\sqrt{2\eta}} \tag{2.6}$$

As an example, at 20 km above sea level (a.s.l) which is the average height of the first interaction of the primary particles, E_{th} for electrons, muons and protons are 67 MeV, 14 GeV and 120 GeV, respectively, while at sea level E_{th} are 22 MeV, 4.6 GeV and 40 GeV, respectively. As expected, the threshold energy for Cherenkov light decreases as the particles penetrate further through the atmosphere.

The number of produced Cherenkov photons N_{ph}, with wavelength between λ_1 and λ_2, per unit of atmospheric depth can be estimated as:

$$\frac{dN_{ph}}{dX_\nu} = 4\pi\alpha\frac{\eta}{\rho}\left(\frac{1}{\lambda_1} - \frac{1}{\lambda_2}\right) \tag{2.7}$$

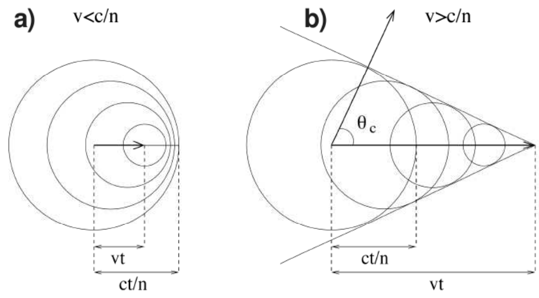

Figure 2.5: Propagation of Cherenkov light in a medium with refractive index n, derived from Huygens' principle..

As it can be seen in Eq. 2.7 the amount of Cherenkov light emitted depends on the atmospheric densitiy profile, ρ. Also, this radiation is mainly concentrated in the near UV and optical band and therefore passes mostly unattenuated to the ground, with losses due to processes that will be discussed in the next section.

2.3.2 Attenuation of photons in atmosphere

Several processes contribute to the absorption of Cherenkov photons before they reach the ground.

- **Rayleigh scattering**

  Rayleigh scattering is the elastic scattering of light by particles smaller than its wavelength (in our case, air molecules whose size is around $10^{-10}\,m$). The transmission coefficient due to Rayleigh scattering is a strong function of the wavelength (λ^{-4} [22]) of the photon, which mainly affects the short wavelength range of the Cherenkov photon spectrum. For atmospheric heights between 3 and 15 km (with perfect weather conditions), Rayleigh scattering is the dominant process for Cherenkov light attenuation.

- **Mie scattering**

  Cherenkov light also suffers scattering through interaction with small dust particles suspended in the air (aerosols, whose size is between $10^{-5}\,m$ for wind-blown dust and $10^{-7}\,m$ for droplets), whose size is comparable to the wavelength of the light. This process is called Mie scattering. The simulation used is based on the model proposed by Elterman [11], which considers an aerosol number density N_p which (roughly) decreases exponentially up to 10 km a.s.l., followed by a more tenuous layer between 10 and 30 km. In this model, the aerosol size distribution is considered to be unchanged with altitude. Since in this model the aerosols are concentrated mainly at very low altitude, the transmission coefficient is more or less constant above a certain height (which depends on zenith angle θ). For instance, for vertically incident 300 nm light emitted higher than 4 km above the telescope, the Mie transmission is about 0.95.

- **Ozone absorption**

  Ozone (O_3 is a molecule widely spread between 10 and 40 km a.s.l. and strongly absorbs photons with wavelengths smaller than 300 nm ($O_3 + \gamma \rightarrow O_2 + O$) .

Most of the Cherenkov light observed at ground is concentrated between 290 nm (ozone cut-off) and around 600-700 nm (drop due to the $1/\lambda^2$ spectral distribution).

Chapter 3

The Simulation and Analysis

3.1 Monte Carlo Simulation

The data analysis in ground-based Cherenkov astronomy requires a dedicated Monte Carlo (MC) simulation of γ-ray and hadron initiated EAS, as well as of the detector response. MC simulations play a critical role in γ-ray astronomy since there is no such thing as a test beam, as for instance in Particle Physics of colliders, and the energy estimation must rely entirely on MC predictions.

The MAGIC Monte Carlo simulation package is divided in three parts. EAS simulation is done with CORSIKA [12], light transport and collection is simulated with the Reflector program [10] and the Camera program [13] takes care of reproducing the detector response.

3.1.1 CORSIKA

The CORSIKA (COsmic Ray SImulations for KAskade) software simulates in detail the evolution of an EAS initiated by photons, protons, nuclei, or any other particle in the atmosphere.

The parameter values needed to steer the production of air showers are provided by the user to the program through an input card.

CORSIKA includes specific routines which simulate the transport of particles in the atmosphere and their decays and interactions with atmospheric nuclei. The atmospheric density profile and the Earth's magnetic field are also considered in the simulation.

All particles are tracked along their path through the atmosphere and the program determines type, energy, location, direction and arrival times of all the particles of the shower that reach a selected observation level, including the Cherenkov photons produced by the charged particles along their path.

The CORSIKA simulation process accounts for the following physical features:

- **Hadronic and electromagnetic interactions**

- **Particle tracking through the atmosphere**: accounts for the ionization energy loss (with the Bethe-Bloch formula) and the deflection by the Earth's magnetic field and the Coulomb multiple scattering.

  There are different atmosphere models implemented in CORSIKA (with composition and density profiles). The atmospheres used in this work are the US Standard Atmosphere and the Magic Winter Atmosphere[1]. Details of these atmospheres can be found at Appendix A.

- **Cherenkov radiation**: the Cherenkov production threshold ($v > c/n$) for charged particles is checked at every step of the trajectory, using the following aproximated expression for the refraction index: $n_h = 1{+}0.000283 \left(\frac{\rho(h)}{\rho(0)}\right)$, where $\rho(h)$ is the atmosphere density value given in Appendix A.

3.1.2 Reflector

The Reflector program accounts for the Cherenkov light absorption and scattering in the atmosphere and the reflection of the surviving photons on the mirror dish.

The Reflector program reads in the files produced by CORSIKA and writes an output file with information about all the photons which reach the telescope focal plane within the camera limits. The production is steered by a specific input card, which includes also the path to the reference input files involved in the reconstruction and the model of atmosphere to be used.

The physical processes considered within Reflector to simulate the atmospheric effects on Cherenkov light propagation are:

- Rayleigh scattering by air molecules.
- Mie scattering by aerosols.
- Absorption by ozone molecules.

3.1.3 Camera

The Camera program simulates the behaviour of the MAGIC photomultipliers, trigger system and data acquisition electronics.

A steering card sets all the relevant parameters of the simulation and the input files (Reflector outputs) to be used.

[1]Densities obtained averaging over 6 month of data available from satellites, which include both latitude and longitude and time. In this case, the MAGIC coordinates and the first day of each month are used

3.2 The Magic Analysis and Reconstruction Software (MARS)

MARS is collection of programs written in C++ in the framework of the ROOT data analysis software maintained at CERN. The aim of MARS is to have a flexible and robust tool to handle all the needs of the analysis in the MAGIC collaboration.

In this section I will describe briefly the main steps of the standard MAGIC analysis chain [14], [23].

3.2.1 Calibration

The process of calibration consists in evaluating the number of photoelectrons recorded by each pixel in every event, taking into account the response of the camera.

The task of calibration is performed by the MARS executable *callisto*, which takes the output of the Camera program as input.

3.2.2 Image cleaning and Image parameterization

After calibration, the next step in the analyisis chain is the parameterization of each shower image by a set of parameters, which are the moments of the light distribution and are called Hillas parameters. A "cleaning" has to be performed in order to remove pixels whose "signals" are basically the result of the fluctuations of the light of the night sky. These tasks are performed in the MAGIC analysis by the program called *star*.

The Hillas parameterization assumes an elliptical shape for the shower image, and uses parameters grouped in two classes: those describing the shape of the shower which are independent on the image location in the camera (SIZE[2], LENGTH, WIDTH,...) and those depending on a reference point in the camera (ALPHA, DIST). In Fig 3.1 the geometrical Hillas parameters are shown. The Hillas parameters that will be discussed throughout this study are [26]:

SIZE Total number of photons in the shower, related to the energy of the primary shower.

ALPHA Angle by which the shower axis misses the Reference Point[3], as seen from the center of the shower image. This is a key parameter that gives information about the incoming direction of the shower, and is small for γ-rays from the source.

[2] More likely to be a parameter of the intensity of light

[3] see Fig. 3.1, it corresponds to the direction of the observed source

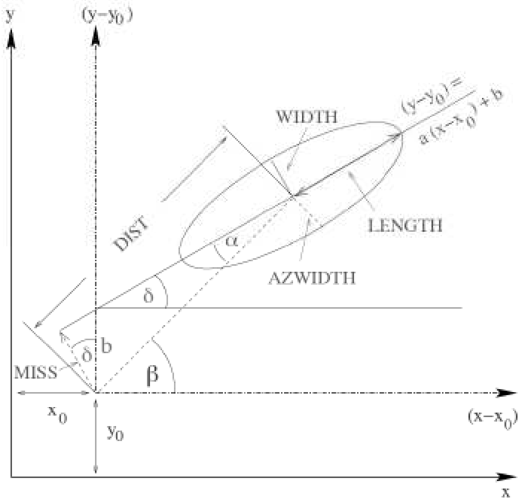

Figure 3.1: Definition of the image parameters. The x,y axes correspond to the camera axis, and (x_0, y_0) is a RP , that represents the source position on the camera.

3.2.3 γ/Hadron separation

The discrimination between background and γ-ray events is based in the different distributions of the image parameters for γ-ray and hadronic showers. The Random Forest method [26] has proved to be a very robust tool to perform the γ/hadron separation. This classification method combines the image parameters into a new one which is a measure of the likelihood of an event to correspond either to a γ-ray or a hadron shower. The *HADRONNESS* parameter has values between 0 and 1, where 0 corresponds to "most-γ-like" and 1 to "most-hadron-like". The Random Forest used in this work was generated by D. Mazin[4].

The last step of the analysis chain is the *melibea* program. This standard MAGIC program uses the RF to estimate the hadronness of the primary gamma-ray (or cosmic ray nucleus) which initiated every one of the showers.

[4] IFAE

Chapter 4

Results

Two samples of MC data have been used: one produced using the US Standard Atmosphere and another one produced using the Magic Winter Atmosphere. These where generated at the CORSIKA level and have the following characteristics:

Magic Winter Atmosphere[1]
Zenith Angle (θ) Range: 10° to 45°
Azimuth Angle (ϕ) Range: 0° to 360°
Energy Range: 30 to 30000 GeV

US Standard Atmosphere[2]
Zenith Angle (θ) Range: 10° to 45°
Azimuth Angle (ϕ): samples at 90°
Energy Range: 10 to 30000 GeV

Fig. 4.1 shows a diagram which summarizes all the steps that have been taken along this work. At the end of this process, the *melibea* output must be treated in order to obtain the effective collection area [26] [24] [23]. The collection area for $\gamma - rays$ is given by the integration of the efficiency over the generation area and may be computed as,

$$A_{\gamma}^{coll}(E, \theta) = \int_{0}^{\infty} P_{\gamma}(E, r, \theta)\, 2\pi r dr \tag{4.1}$$

where the efficiency (with energy E and impact parameter r) is defined as,

$$P_{\gamma}(E, r, \theta) = \frac{events\, after\, the\, analysis}{total\, number\, of\, events\, simulated}$$

[1]MC sample provided by J. Sitarek (*Max-Planck-Institut fűr Physik*)
[2]MC sample obtained from PIC Data Center, Bellaterra

If the MC has been generated homogeneously in x and y (coordinates on the ground of the shower core), this is equivalent to

$$A_{\gamma}^{coll}(E,\theta) = \langle\frac{n_{survived}}{n_{simulated}}\rangle(E,\theta)A_{gen}(E,\theta)$$

with $A_{gen}(E,\theta) = \pi r_{max}^2(E,\theta)$ the total area of the MC generation, and r_{max} the maximum impact parameter considered in this simulation. All this process is done by a MARS macro called *collarea.C*. At this level, in collarea's code, one is able to perform all the necessary cuts as, for instance, hadronness, alpha, azimuth angle. The cut in azimuth angle must be done in order to have the same range in both atmospheric MC sample, moreover, the same analysis performed with the US atmosphere will be done to the MW atmosphere.

In the MAGIC analysis, the background suppression is achieved by applying an upper cut in hadronness (see Chapter 3). In the analysis of real data, this is necessary to make tiny gamma-ray signals visible above the background fluctuations. A further cut in ALPHA will select the events coming from the direction of the candidate γ-ray source

According to the standard procedures in MAGIC analysis, I selected to perform two constant cuts in Hadronness (0.1 and 0.2) and Alpha (10° and 12°), and, also, two cuts in efficiency. To perform these non-constant cuts I divided the event sample in bins of SIZE. For every one of these bins, I determine the hadronness at which keeps a given fraction of gammas. To see it more clearly I will refer to Fig. 4.2 (a), where a cut in hadronnes of 60% is enforced: in every bin one counts the number of events along the Y axis (hadronness in this case), and marks where the 60% of the events with lower hadronness (see the red cross symbol in the plot) is expected. Once this process is done for every one of the bins, I fit a function (see Eq. 4.2) to all the points, which will determine the non-constant cut to be performed in *collarea.C*.

Note that the fixed cuts reject most of the gammas at low Sizes, hence effectively increasing the threshold of the telescope. The constant-efficiency cuts are used to circumvent this problem and are parametrized as follows:

$$Y = [p0] + [p1]\left(\frac{1}{2} + \frac{1}{2}tanh(-[p2](X - [p3]))\right) \tag{4.2}$$

where Y is either Hadronness or Alpha and X is Size. The parameters [p0],[p1],[p2],[p3] will be given in every plot. As said before, these same cuts will be used with the MW sample. The Figs. 4.2 and 4.3 represent all the events as a function of hadronness, alpha and size.

The representation of the γ-ray collection areas for the two atmospheres and the ratio between the two collection areas are given in Figs. 4.4 and 4.5. This ratio is represented by the symbol Q_{MW}^{US} which symbolizes the division of the collection area obtained with the US Standard Atmosphere sample by the collection area for the Magic Winter Atmosphere.

As it was mentioned before, we want to estimate the implications of considering US Atmosphere (implemented in the MAGIC analysis) instead of the Magic Winter (which is in principle more similar to the real atmosphere in La Palma). These possible implications can be noticed on the final Crab Nebula spectrum that we obtained for both atmospheres. In the following we will assume that the Crab spectrum is a pure power-law[3]:

$$\frac{dJ_\gamma}{dE} = (2.83 \pm 0.04) \times 10^{-14} \left(\frac{E}{GeV}\right)^{-2.62\pm0.02} \left[\frac{ph}{cm^2 sGeV}\right] \tag{4.3}$$

Hence, if for the US Atmosphere one has $\frac{dJ_\gamma^{US}}{dE} = \frac{dN_\gamma}{dE\,dt\,dA^{US}}$, for for the MW Atmosphere $\frac{dJ_\gamma^{MW}}{dE} = \frac{dN_\gamma}{dE\,dt\,dA^{MW}}$. Multipliying the previous equation for MW by Q_{MW}^{US} and considering $A^{MW} = 1$ we obtain the first equation for US, hence the spectrum for the MW atmosphere can be derived from the US as:

$$\frac{dJ_\gamma^{MW}}{dE} = \frac{dJ_\gamma^{US}}{dE} \cdot Q_{MW}^{US}$$

Therefore, to obtain the change in the spectrum I just have to multiply the spectrum from Eq. 4.3 with the ratio Q_{MW}^{US}. Figs. 4.6, 4.7, 4.8 and 4.9 give an outlook of the observed change. Additionally, in these graphics a fit, in energy range from 100 GeV to 20 TeV, of the new Crab Spetrum has been performed:

$$\frac{dJ_\gamma}{dE} = [p0] \left(\frac{E}{1000}\right)^{[p1]} \tag{4.4}$$

The parameters [p0] and [p1] will be given in every plot.

[3] This is not exactly true, but our aim is just to test the effect of the atmosphere on a typical (power-law) source spectrum

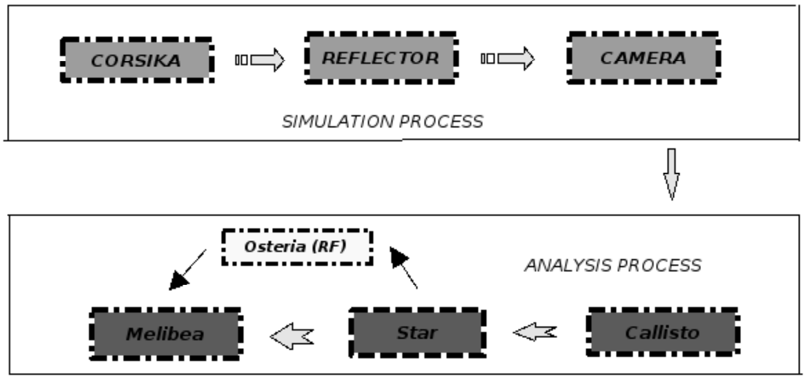

Figure 4.1: The MAGIC Simulation and Analysis chain.

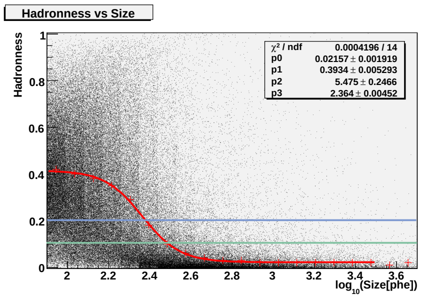

(a) Cut in *Hadronness* of 60% for US Std.

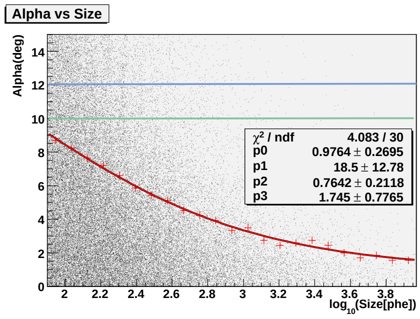

(b) Cut in *Alpha* of 70% for US Standard.

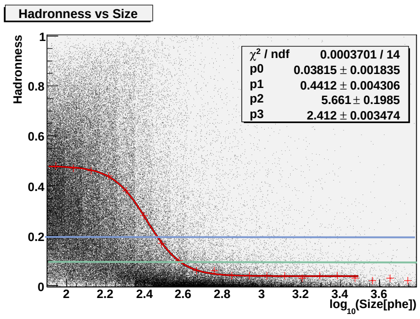

(c) Cut in *Hadronness* of 70% for US Std.

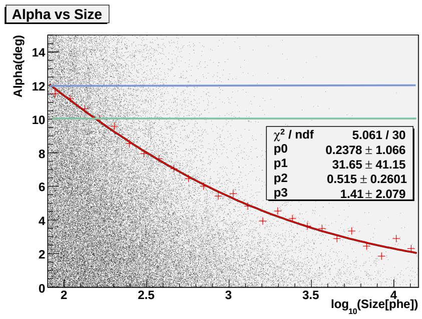

(d) Cut in *Alpha* of 85% for US Standard.

Figure 4.2: Cuts in *Hadronness* and *Alpha* for the US Standard Atmosphere for zenith angle between 10° and 30°. The constant cuts are also plotted (horizontal lines).

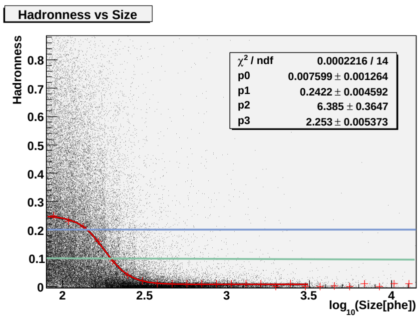

(a) Cut in *Hadronness* of 60% for US Std.

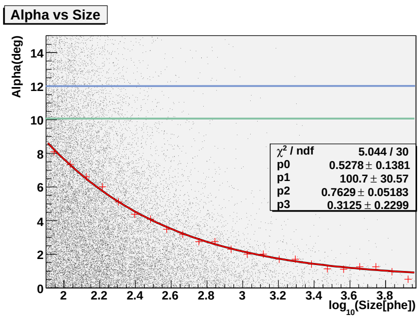

(b) Cut in *Alpha* of 70% for US Standard.

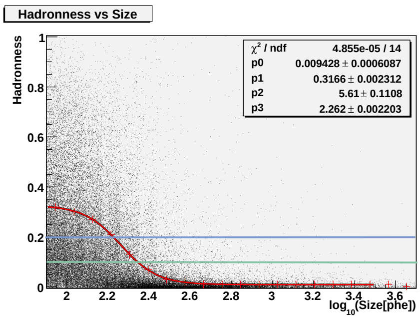

(c) Cut in *Hadronness* of 70% for US Std.

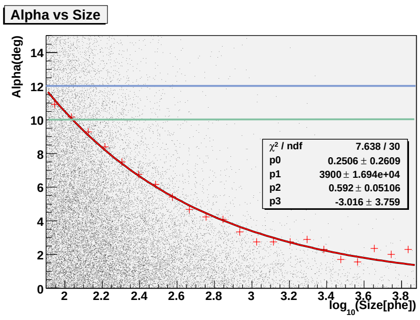

(d) Cut in *Alpha* of 85% for US Standard.

Figure 4.3: Cuts in *Hadronness* and *Alpha* for US Standard Atmosphere for zenith angle between 30° and 45°. The constant cuts are also plotted (horizontal lines).

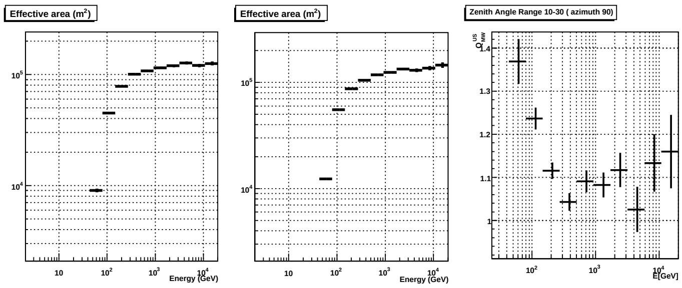

(a) *Hadronness* 0.1 *Alpha* 10°.

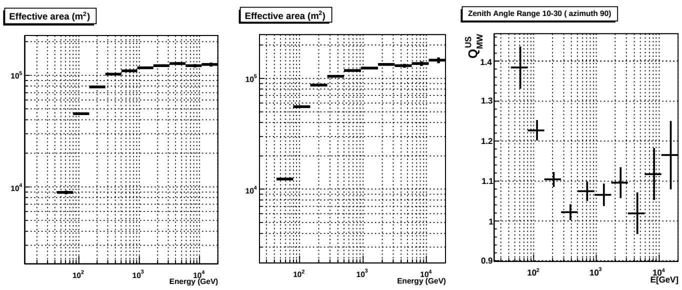

(b) *Hadronness* 0.2 *Alpha* 12°.

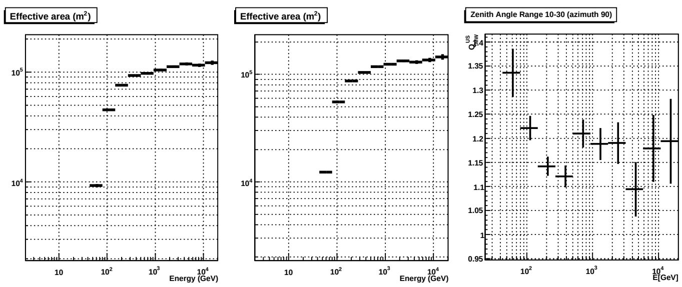

(c) *Hadronness* of 60% *Alpha* 70%.

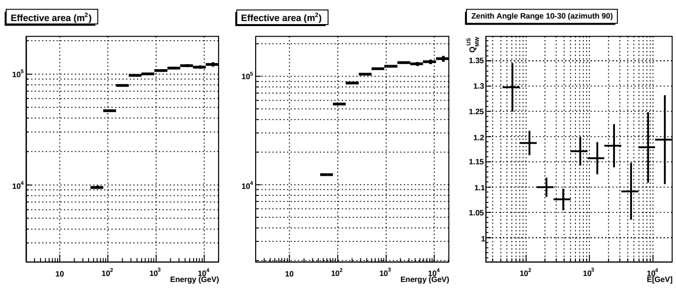

(d) *Hadronness* 70% *Alpha* 85%.

Figure 4.4: In this figure the collection areas (range 10° to 30°) for Magic Winter (left) and US Std (centre) are represented. Also the ratio between both areas is given (right).

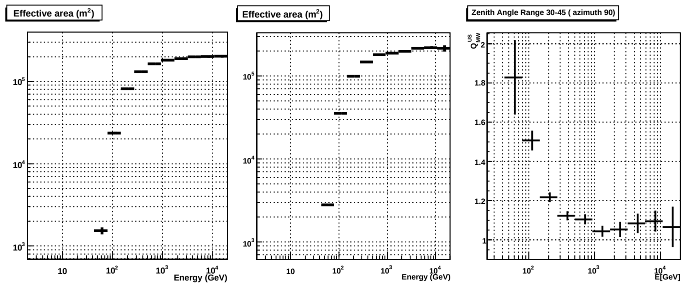

(a) *Hadronness* 0.1 *Alpha* 10°.

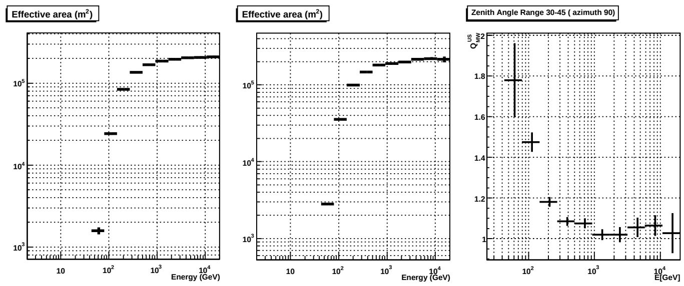

(b) *Hadronness* 0.2 *Alpha* 12°.

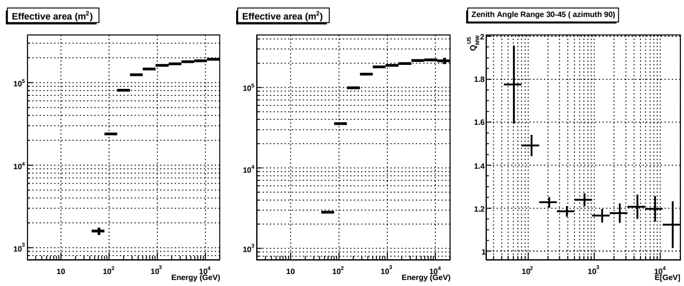

(c) *Hadronness* of 60% *Alpha* 70%.

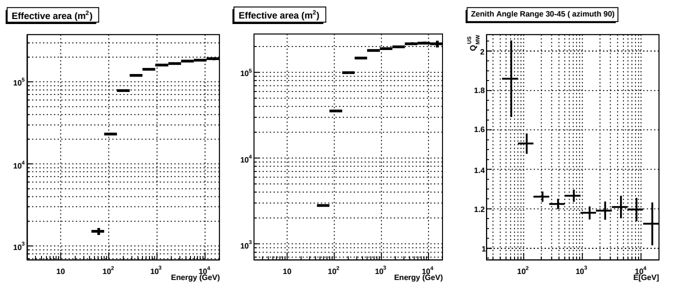

(d) *Hadronness* 70% *Alpha* 85%.

Figure 4.5: In this figure the collection areas (range 30° to 45°) for Magic Winter (left) and US Std (centre) are represented. Also the ratio between both areas is given (right).

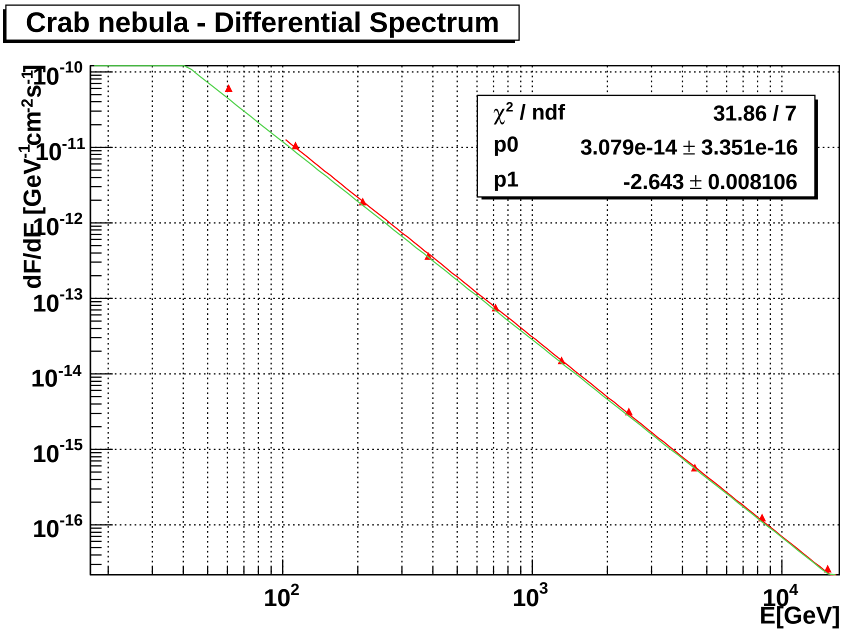

(a) *Hadronness* 0.1 *Alpha* 10°.

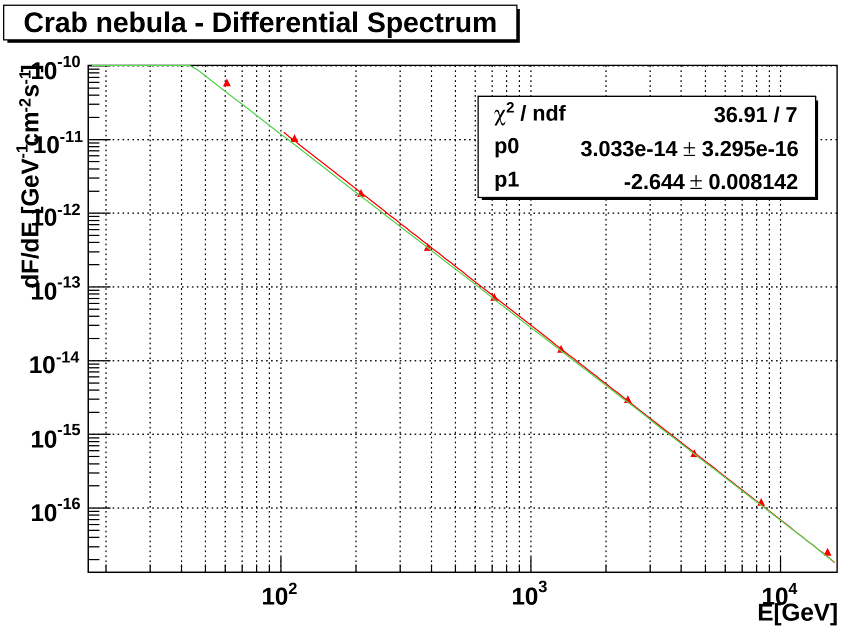

(b) *Hadronness* 0.2 *Alpha* 12°.

Figure 4.6: Crab Nebula differential energy spectra (*green line*) and its modification due to the change in atmosphere (*red line*) for zenith angle range 10° to 30° and constant cuts.

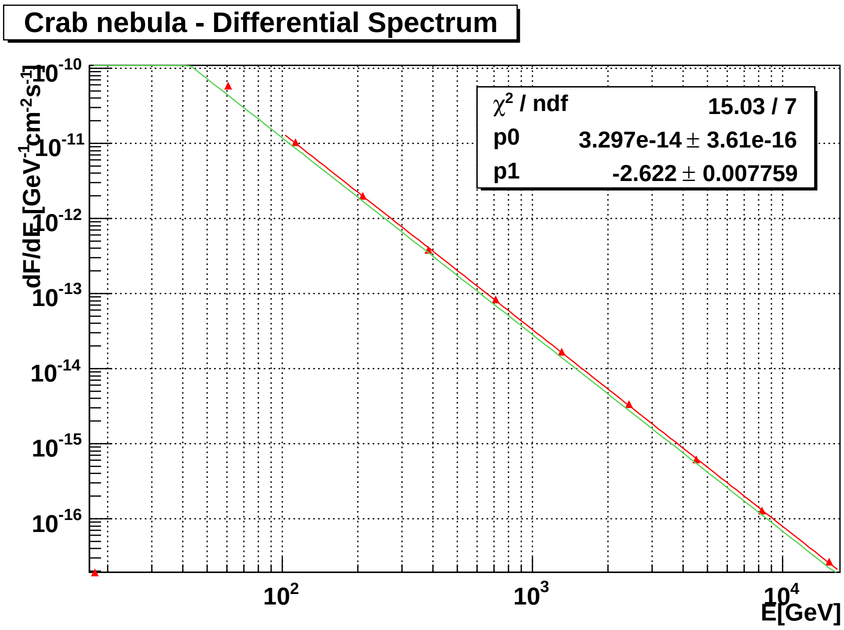

(a) *Hadronness* 60% *Alpha* 70%.

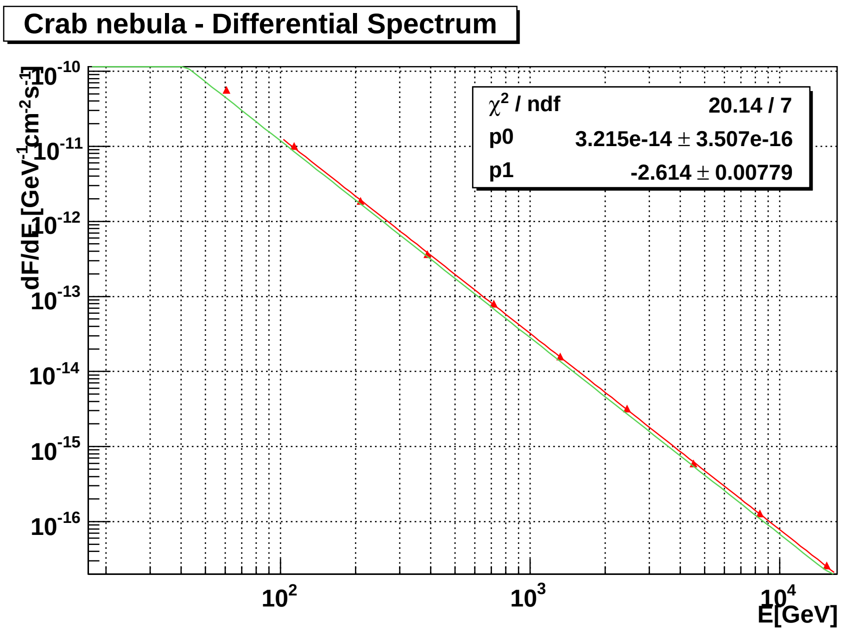

(b) *Hadronness* 70% *Alpha* 85%.

Figure 4.7: Crab Nebula differential energy spectra (*green line*) and its modification due to the change in atmosphere (*red line*) for zenith angle range 10° to 30° and cuts in efficiency.

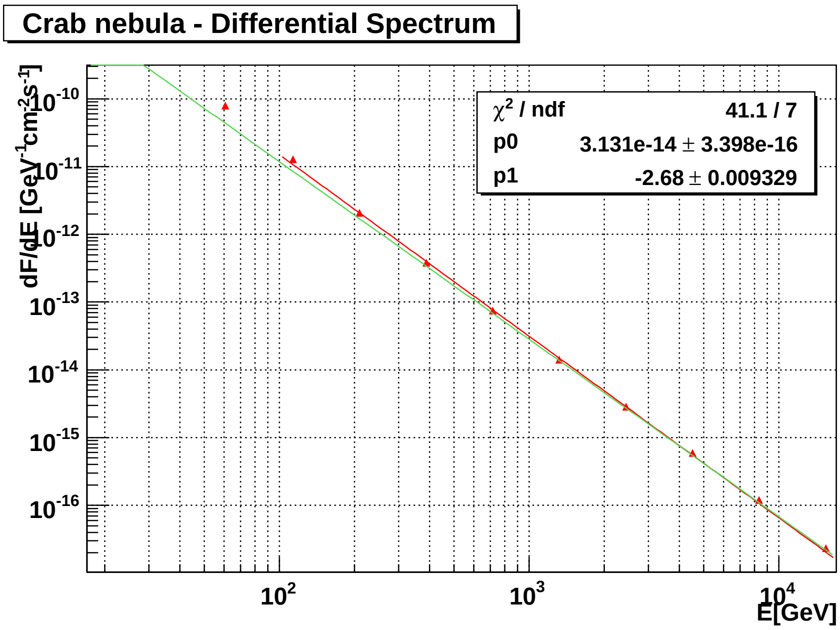

(a) *Hadronness* 0.1 *Alpha* 10°.

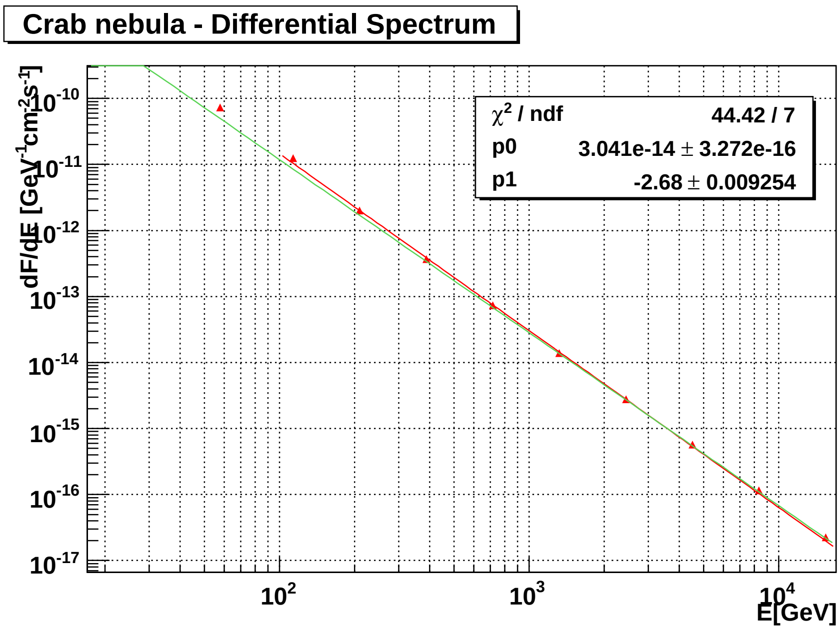

(b) *Hadronness* 0.2 *Alpha* 12°.

Figure 4.8: Crab Nebula differential energy spectra (*green line*) and its modification due to the change in atmosphere (*red line*) for zenith angle range 30° to 45° and constant cuts.

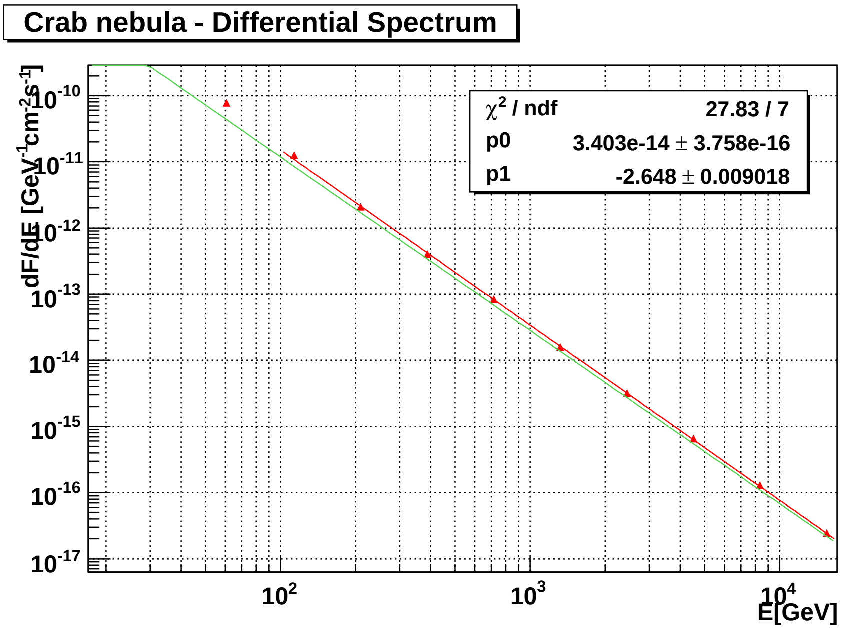

(a) *Hadronness* 60% *Alpha* 70%.

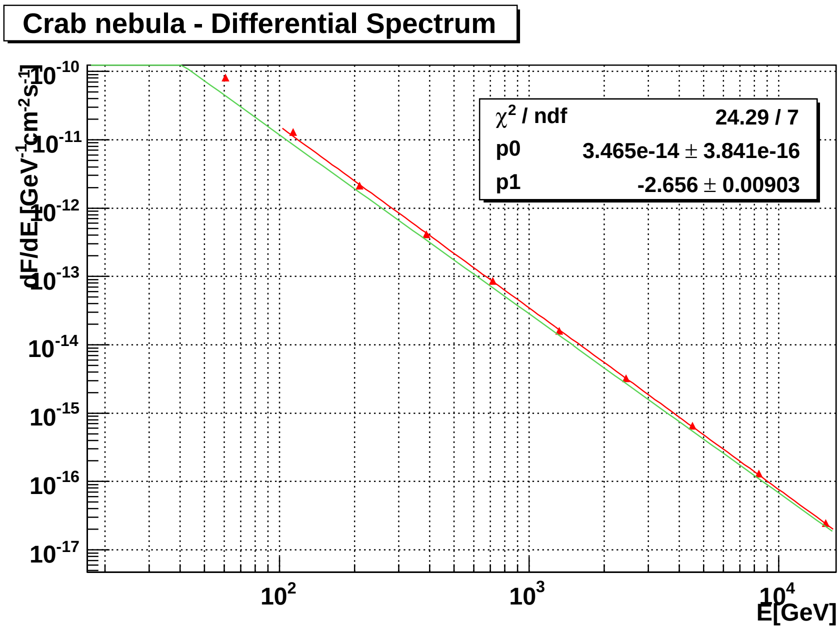

(b) *Hadronness* 70% *Alpha* 85%.

Figure 4.9: Crab Nebula differential energy spectra (*green line*) and its modification due to the change in atmosphere (*red line*) for zenith angle range 30° to 45° and cuts in efficiency.

Chapter 5

Discussion and Conclusions

- **Discussion**

  The differences obtained between the collection areas of US Standard Atmosphere and Magic Winter Atmosphere, which are established by Q^{US}_{MW}, have a good agreement with the predictions obtained by previous studies [16], in which a decrease of 10-15% in the Cherenkov photon density was observed for the Magic Winter atmosphere compared with the US Standard atmosphere. This is related with our study in the sense that lower light density results in a reduced γ-ray collection area.

  In the two studied ZA ranges, a high difference between the atmosphere on Q^{US}_{MW} can be observed at low energies. This is due to the fact that when the amount of light is close to the threshold of observation, any slight variation of light (towards smaller values) reduces considerably the number of events, which is translated in a quick drop of the effective collection area. Obviously, this effect is less accused in the plateau regime, generally above 200 GeV.

  Additionally, the values of Q^{US}_{MW} obtained for the ZA range 30° to 45° are higher than those derived from ZA range 10° to 30°. This effect is due to the fact that for higher ZA the distance between the first point of interaction of the γ-ray with the atmosphere and the observation point is longer than for lower ZA, and, therefore, there is a higher influence of the atmosphere because of the larger absorption.

  The "modified" Crab Nebula Differential Spectra have been fitted for energies above 10^2 Gev, because above this value the behaviour is more similar to a power-law. Compared with the usual Crab Spectrum, there are no remarkable differences[1] with the new produced spectrum. Nevertheless, differences of around 10% (see, for instance, plots of the rate of collection areas) between the results obtained after constant cuts and those from

[1] To be comented in next section

non-constant cuts have been observed. More precise studies to identify this effect are still to be done, nevertheless it can be mentioned that applying a non-constant cut in the MW sample, using the same cut that was used for the US sample, means considering a different efficiency, and, therefore, the differences in the results can be ascribed to this fact.

Finally, in this study the lack of statistics has been a problem in order to give a better precision in the final Q_{MW}^{US}. The fact that MC for Magic Winter was generated for a azimuth angle range of 0° to 360° and, consequently, I had to perform a cut in the azimuth angle in order to match with the data available for US Standard, made the statistics of these results quite low. The importance of this cut is due to the fact that, as many studies prove [19] [21], there is a difference in the collection area for different azimuth angles, due to the different effect of the Earth's magnetic field.

- **Conclusions**

This study estimates the effect of the atmosphere on the energy spectrum by means of comparing the effective collection area for two different atmospheres, the Magic Winter Atmosphere and the US Standard Atmosphere. Briefly, the physics involved in the IACT experiments, the simulation process and the analysis techniques used are reviewed.

Results from the Monte Carlo simulations in this study lead to one conclusion: changing the molecular atmospheric density profile, from US Standard Atmosphere to Magic Winter Atmosphere, in the MAGIC MC simulation software, does not alter remarkably the spectrum of a γ-ray source except at low energies close to the threshold.

From the final fit of the "new" Spectrum obtained with the MW Atmosphere it can be seen how this spectrum is slightly displaced in upward direction from the one derived with the US Atmosphere. This effect, which already has been discussed before, is not as remarkable as the fact that the slope (see parameter [1] in the spectrum plots) remains almost unchanged, and only just a 1% of change is observed for the lower zenith angle range, while for the higher a 2% is obtained.

As stated before, it would be desirable to continue this study with more data available. It would be also interesting to perform studies with different atmospheres, besides US and MW, and, moreover, do a similar study considering the influence of the aerosol distribution.

Finally comment that future arrays of telescopes, due to the huge amount of data available, will certainly reduce the statistycal errors. Therefore, having a good caracterization of the atmosphere will be determinant in order to push down with the systematic errors.

Acknowledgments

I am very thankful to my supervisors Lluis Font and Abelardo Moralejo for all their dedication to this project. Despite their busy schedules, they always found time to help me.

I am especially grateful to the tireless help that Manel Errando offered me since I got involved with this project. Most of the macros needed for the analysis that I developed throught this work were due to his priceless help (I still owe him a couple of beers). I am also very thankful to the younger PhD students like Daniela Hadasch, who, as my colleague, was always happy to offer me a quick solution for my problems, and also to Ignasi Reichardt, who also helped me to understand the language of ROOT.

I would also like to thank Julian Sitarek for providing me with the MC sample for MW, and Daniel Mazin for providing me with the RF and helping me in developing some of the macros nedeed for the analysis.

Thanks to all the MAGIC collaboration for opening me the doors to the beauty of Astroparticle physics.

Finalment, m'agradaria agraïr sincerament el suport i l'estima que he rebut per part del meus pares, com també de la resta de la meva família i dels meus amics i amigues. I also have special thanks for Anna Lisa who always stayed close to me and supported me in difficult times.

Appendix A

Atmospheric Models

Atmospheric Model 6 (U.S. Standard)			
1	**2**	**3**	**4**
Alt [km]	**rho** [g/cm^3]	**thick** [g/cm^2]	**n-1**
0.000	0.12219E-02	0.10350E+04	0.28232E-03
1.000	0.11099E-02	0.91853E+03	0.25634E-03
2.000	0.10054E-02	0.81286E+03	0.23214E-03
3.000	0.90839E-03	0.71725E+03	0.20975E-03
4.000	0.81888E-03	0.63097E+03	0.18904E-03
5.000	0.73643E-03	0.55328E+03	0.16994E-03
6.000	0.66012E-03	0.48352E+03	0.15235E-03
7.000	0.59048E-03	0.42105E+03	0.13620E-03
8.000	0.52609E-03	0.36529E+03	0.12136E-03
9.000	0.46741E-03	0.31567E+03	0.10782E-03
10.000	0.41370E-03	0.27167E+03	0.95426E-04
11.000	0.36499E-03	0.23278E+03	0.84194E-04
12.000	0.31209E-03	0.19900E+03	0.71987E-04
13.000	0.26674E-03	0.17012E+03	0.61523E-04
14.000	0.22792E-03	0.14543E+03	0.52581E-04
15.000	0.19479E-03	0.12434E+03	0.44937E-04
16.000	0.16651E-03	0.10631E+03	0.38406E-04
17.000	0.14236E-03	0.90902E+02	0.32840E-04
18.000	0.12168E-03	0.77727E+02	0.28071E-04
19.000	0.10403E-03	0.66465E+02	0.23997E-04
20.000	0.88928E-04	0.56837E+02	0.20516E-04
21.000	0.75750E-04	0.48620E+02	0.17475E-04
22.000	0.64544E-04	0.41621E+02	0.14887E-04
23.000	0.55021E-04	0.35655E+02	0.12695E-04
24.000	0.46965E-04	0.30566E+02	0.10833E-04
25.000	0.40097E-04	0.26222E+02	0.92494E-05
27.500	0.27126E-04	0.17925E+02	0.62570E-05
30.000	0.18420E-04	0.12302E+02	0.42495E-05
32.500	0.12139E-04	0.85361E+01	0.28004E-05
.	.	.	.
.	.	.	.
.	.	.	.
80.000	0.18430E-07	0.10993E-01	0.42513E-08
85.000	0.82291E-08	0.46676E-02	0.18985E-08
90.000	0.34321E-08	0.19250E-02	0.79163E-09
95.000	0.14063E-08	0.78968E-03	0.32437E-09
100.000	0.57185E-09	0.32602E-03	0.13189E-09
105.000	0.24206E-09	0.13421E-03	0.55841E-10
110.000	0.10312E-09	0.52792E-04	0.23788E-10
115.000	0.46595E-10	0.17216E-04	0.10748E-10
120.000	0.24596E-10	0.00000E+00	0.56734E-11

Figure A.1: The US Standard Atmosphere

Atmospheric Model 11 (MagicWinter)			
1	**2**	**3**	**4**
Alt [km]	**rho** $[g/cm^3]$	**thick** $[g/cm^2]$	**n-1**
0.000	0.12167E-02	0.10526E+04	0.28047E-03
1.000	0.10996E-02	0.93687E+03	0.25348E-03
2.000	0.99545E-03	0.83221E+03	0.22947E-03
3.000	0.90172E-03	0.73744E+03	0.20786E-03
4.000	0.81648E-03	0.65159E+03	0.18821E-03
5.000	0.73831E-03	0.57390E+03	0.17019E-03
6.000	0.66616E-03	0.50373E+03	0.15356E-03
7.000	0.59932E-03	0.44050E+03	0.13815E-03
8.000	0.53726E-03	0.38370E+03	0.12385E-03
9.000	0.47967E-03	0.33289E+03	0.11057E-03
10.000	0.42631E-03	0.28762E+03	0.98271E-04
11.000	0.37696E-03	0.24749E+03	0.86896E-04
12.000	0.33127E-03	0.21211E+03	0.76363E-04
13.000	0.28903E-03	0.18112E+03	0.66627E-04
14.000	0.25022E-03	0.15419E+03	0.57680E-04
15.000	0.21485E-03	0.13097E+03	0.49528E-04
16.000	0.18304E-03	0.11111E+03	0.42194E-04
17.000	0.15504E-03	0.94234E+02	0.35739E-04
18.000	0.13087E-03	0.79970E+02	0.30167E-04
19.000	0.11030E-03	0.67940E+02	0.25425E-04
20.000	0.92983E-04	0.57801E+02	0.21434E-04
21.000	0.78510E-04	0.49248E+02	0.18098E-04
22.000	0.66403E-04	0.42020E+02	0.15307E-04
23.000	0.56250E-04	0.35902E+02	0.12967E-04
24.000	0.47719E-04	0.30716E+02	0.11000E-04
25.000	0.40536E-04	0.26314E+02	0.93442E-05
27.500	0.27101E-04	0.17977E+02	0.62473E-05
30.000	0.18239E-04	0.12385E+02	0.42045E-05
32.500	0.12346E-04	0.86110E+01	0.28461E-05
45.000	0.19671E-05	0.16336E+01	0.47192E-06
50.000	0.11066E-05	0.87176E+00	0.25508E-06
55.000	0.60722E-06	0.45550E+00	0.13997E-06
60.000	0.32484E-06	0.22908E+00	0.74880E-07
65.000	0.16606E-06	0.11024E+00	0.38280E-07
70.000	0.80685E-07	0.50835E-01	0.18599E-07
75.000	0.37549E-07	0.22540E-01	0.86557E-08
80.000	0.15268E-07	0.95236E-02	0.35196E-08
85.000	0.69409E-08	0.42575E-02	0.16000E-08
90.000	0.32565E-08	0.18272E-02	0.75069E-09
95.000	0.14484E-08	0.69690E-03	0.33388E-09
100.000	0.52180E-09	0.23438E-03	0.12028E-09
105.000	0.15993E-09	0.80789E-04	0.36866E-10
110.000	0.53349E-10	0.33136E-04	0.12297E-10
115.000	0.28310E-10	0.14282E-04	0.65260E-11
120.000	0.21253E-10	0.00000E+00	0.48990E-11

Figure A.2: The Magic Winter Atmosphere

Bibliography

[1] V.Hess. Observation of penetrating radiation of seven ballon flights. *Physikalische Zeitschrift*, 13:1084, 1912

[2] J. Kildea et al. The Whipple Observatory 10 m gamma-ray telescope, 1997 2006. *Astroparticle Physics*, 28:182-195, October 2007.

[3] M. S. Longair. *High Energy Astrophysics, Particles, Photons and Their Detection*, volume 1. Cambridge University Press, 2 edition, February 1992.

[4] T. M. Kneiske. Gamma-ray background: a review. *ArXiv e-prints*, 707, July 2007.

[5] F. A. Aharonian. *Very High Energy Cosmic Gamma Radiation*. World Scientific, 2004.

[6] S. Nolan, M. Daniel. *Testing the Effect of Atmosphere on a CTA-Type*. Durham University.

[7] T. K. Gaisser. *Cosmic Rays and Particle Physics*. Cambridge University Press.

[8] P.A. Cherenkov. *Dokl. Akad. Nau, SSSR,* 2:451, 1934.

[9] I.Frank, I. Tamm, and C.R. Acad. *Sci. URSS*, 14:109, 1937.

[10] A. Moralejo. *The Reflector Simulation Program v.0.6.* 2002, MAGIC-TDAS 02-11

[11] L. Elterman. *Applied Optics Vol.3, No 6 (1964) 745.*

[12] D. Heck and J. Knapp. *EAS Simulation with CORSIKA: A User's Manual.* 2002

[13] O. Blach, A. Moralejo. *How to Use the Camera Simulation Program 0.7.* 2004, MAGIC-TDAS 04-07

[14] M. Gaug, A. Moralejo. *A handbook of the standard MAGIC analysis chain.* 2008, MAGIC-TDAS 08-02

[15] *The importance of atmosphere monitoring in Cherenkov experiments*. 2002. J.L Osborne, M. Aye, P.M. Chadwick, M.K. Daniel, T.J.L. McComb, J.M. McKenny, S.J. Nolan, K.J. Orford and S.M. Rayner. University of Durham. Bull. Astr. Soc. India (2002) 30, 51-59.

[16] A. Biland, M. Haffke, P. Majumdar, D. Sobczynska and V. Vitale. *Monte Carlo Production Strategy for MAGIC-II Two-Telescope System*. MAGIC Internal Note: TDAS 12-06. 2006

[17] D. Dorner, K. Nilsson, and T. Bretz. *A method to correct IACT data for atmospheric absorption due to the Saharan Air Layer*. A&A 493, 721-725 (2009).

[18] A. Moralejo and M. Gaug. *Software Coordinator's Report*. Collaboration Meeting, Elba 2009.

[19] S. Lobardi. *Implementation in MARS of the Azimuthal dependence of the Effective Area*. MAGIC Sofware premeeting, Elba 2009.

[20] D. Hrupec. *Plans for simulations within MAGIC*. MAGIC meeting, Padua, 2008.

[21] S. Comminchau and A. Biland. *Geomagnetic field effects on the imaging technique*. MAGIC-TDAS 07-04

[22] C.F. Bohren and D.Huffman. *Absorption and scattering of light by small particles*. John Wiley, New York, 1983.

[23] M. Gaug. *Ph.D Thesis: Calibration of the MAGIC Telescope and Observation of Gamma Ray Bursts*. Universitat Autnoma de Barcelona, March 2006.

[24] R. Firpo. *Treball de recerca de Tercer Cicle: Study of MAGIC Telescope sensitivity for Large Zenith Angle observations*. Universitat Autnoma de Barcelona and IFAE, September 2005.

[25] D. Hadasch. *Diploma thesis: Study of the MAGIC performane at high zenith angles and application of the results on a very high energy gamma ray flare of the blazar PKS 2155-305*. Universität Dortmund, August 2008.

[26] M. Hayashida. *Ph.D thesis: Observation of Very-High-Energy Gamma-Rays from Blazars with the MAGIC Telescope*. Universität Műnchen, 2008.

[27] M. Errando. *Treball de recerca de Tercer Cicle: Study of optical properties of last generation photodetectors for Cherenkov astronomy applications*. Institut de Fsica d'Altes Energies and Universitat Autnoma de Barcelona, October 2006.